FERMILAB-PUB-23-795-STUDENT

Weak Gravitational Lensing of Low Surface Brightness Galaxies in the DES Year 3 Catalog

N. Chicoine★, J. Prat, G. Zacharegkas, C. Chang, D. Tangolidis, A. Drlica-Wagner,
(The DES Collaboration)

5 December 2023

ABSTRACT

We present galaxy-galaxy lensing measurements of a sample of low surface brightness galaxies (LSBGs) drawn from the Dark Energy Survey Year 3 (Y3) data. LSBGs are diffuse galaxies with a surface brightness dimmer than the ambient night sky. Given their faintness, the use of standard observational techniques proves challenging. Weak gravitational lensing probes both the baryonic and dark matter content of galaxies, rendering it a powerful technique to estimate LSBG masses. The LSBG lens sample consists of 23, 790 total extended galaxies separated into red and blue color types at $g - i \geq 0.60$ and $g - i \leq 0.60$, respectively. We use the Y3 Metacalibration shape catalog as the source sample, with a number density of $5.59\mathrm{gal/arcmin}^2$. We measure the tangential shear around the lens galaxies across angular scales of $0.25 - 400$ arcmin and find a signal-to-noise of 6.67 for red galaxies, 2.17 for blue galaxies, and 5.30 for the total sample. We fit a model built from two NFW profiles corresponding to the LSBG dark matter subhalo and host halo to the red LSBG shear measurements with an MCMC. We estimate the host halo mass at $7.3^{+2.0}_{-1.6} \times 10^{12} M_{\odot}$. We place a 95% upper bound on the subhalo mass at $2.8 \times 10^{11} M_{\odot}$. We utilize the lens sample photometry to obtain an estimate of the red LSBG stellar mass distribution. We compare the ratio between the stellar mass and the subhalo mass to the parameterized, satellite-specific SHMR (Moster et al. 2010). This work represents the first example of an attempted constraint on the masses of LSBGs using weak gravitational lensing.

1 INTRODUCTION

Low-surface-brightness galaxies (LSBGs) are diffuse, usually dark-matter dominated galaxies colloquially defined by a surface brightness fainter than the ambient night sky. Recent interest in LSBGs has grown due to the critical role they play in understanding galaxy evolution (Thuruthipilly et al. 2023). These galaxies reside in extended dark matter halos and frequent environments ranging from the open field to massive galaxy clusters (Bothun et al. 1997; McConnachie 2012; Martin et al. 2013; Danieli et al. 2017; Cohen et al. 2018; Leisman et al. 2017; Prole et al. 2021). Their diversity extends to their size range: they can appear as compact as dwarf galaxies or stretch to five times the size of the Milky Way (Das 2013; Kado-Fong et al. 2021; Greene et al. 2022). Though current estimates indicate that LSBGs contribute little to the observable universe's stellar mass density and luminosity (<10%) (Bernstein et al. 1995; Driver 1999; Hayward et al. 2005; Martin et al. 2019), they may account for a sizable fraction of the total number density of galaxies (30% - 60%) and hold significant sway over the physics of galaxy evolution (McGaugh 1996; Bothun et al. 1997; O'Neil & Bothun 2000; Minchin et al. 2004; Martin et al. 2019). Notable catalogs of LSBGs have been produced by Rosenbaum et al. (2009); Greco et al. (2018); Tanoglidis et al. (2021). The faintness of these aptly-named galaxies makes direct observation challenging, but their extreme characteristics present an opportunity to probe the nature of dark matter and test current theories of galaxy evolution.

Examining LSBG masses can provide a clearer picture of the stellar-to-halo-mass relation (SHMR) (Du et al. 2020). The SHMR describes the connection between the mass of dark matter halos and their resident galaxies (Moster et al. 2010; Behroozi et al. 2010). Comparing LSBGs to the general, parameterized SHMR tests the limits and the scope of the relation and provides information on the connection between stellar and dark matter mass in LSBGs (Niemiec et al. 2022).

Gravitational lensing presents a promising avenue for studying LSBGs. Gravitational lensing occurs when light from a background object, such as a star or galaxy cluster, passes by the gravitational potential well of a foreground mass (Bartelmann 2010). The foreground mass (lens object) perturbs the light from the background mass (source object), creating a distorted image. This distortion can occur in terms of both shape and size, or shear and magnification. The larger the lens mass, the deeper the gravitational well, and the greater the distortion. As such, gravitational lensing traces both the dark and baryonic matter composition of the lens object. We utilize galaxy-galaxy lensing, in which both the background and foreground objects are galaxies. Though the lensing effect for a single galaxy-galaxy pair is negligible, we can find a preferred tangential alignment of source galaxies around lens galaxies with large counts of lens-source pairs (Bartelmann & Maturi 2017). In other words, the major axes of the ellipses of the source galaxy images orient tangentially around the lens galaxy images, creating a tangential shear. This work represents the first example of using weak lensing to constrain the masses of LSBGs.

2 DATA

2.1 Lens Catalog

We use a lens sample of LSBGs selected from the Dark Energy Survey Year 3 (DES Y3) images (Sevilla-Noarbe et al. 2021) and described in detail in Tanoglidis et al. (2021). Tanoglidis et al. (2021) refined the sample with a series of cuts to reject artifacts and reduce

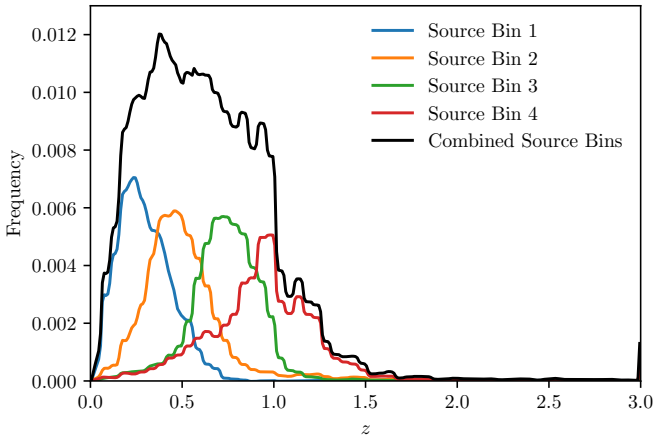

Figure 1. Redshift distribution of source galaxies, with a mean redshift of 0.6312 for the full sample. The four redshift bins are weighted by galaxy count, summed, and normalized to produce the combined source bin distribution.

imaging contamination. Point-like objects (as identified by SourceExtractor) were removed and cuts were applied to define extended LSBGs as galaxies with g-band effective radii of

$$R_{\rm eff}(g) > 2.5\text{arcsec}$$

and a mean surface brightness of

$$\mu_{\rm eff}(g) > 24.3 \frac{\rm mag}{\rm arcsec^2}.$$

The sample was further color-restricted to the ranges:

$$-0.1 < (g-i) < 1.4 \quad (1)$$

$$(g-r) \geq 0.7 \times (g-i) - 0.4 \quad (2)$$

$$(g-r) \leq 0.7 \times (g-i) + 0.4. \quad (3)$$

Objects in the sample were required to have an ellipticity ≤ 0.7 to remove high-ellipticity artifacts (i.e. diffraction spikes). The average angular number density of LSBGs in the Tanoglidis et al. (2021) sample stands at $4.5\text{gal}/\text{deg}^2$.

Galaxy colors correlate with galactic stellar populations, morphologies, and environments. In large surveys, galaxy color distributions are bimodally split into red and blue color categories (Blanton et al. 2003). Tanoglidis et al. (2021) separated the LSBGs at $g-i = 0.60$ in fig. V, dividing red galaxies at $g-i \geq 0.60$ (7,805 galaxies) and blue galaxies at $g-i < 0.60$ (15,985 galaxies). We follow this same division. As seen in fig. VIII of Tanoglidis et al. (2021), the red galaxies are strongly clustered, while the blue galaxies are scattered across the field.

2.2 Source Catalog

The background sources come from the Y3 Metacalibration shape catalog described in Gatti et al. (2021). The redshift distribution of this catalog and its uncertainties are calibrated with the Self Organizing Maps Photometric Redshifts, or SOMPZ (Myles & Alarcon et al., 2021). The resulting redshift distribution shapes are further constrained using the clustering redshifts (WZ) method (Giannini et al. 2022). The Y3 Metacalibration shape catalog includes four tomographic redshift bins. To reduce the shape noise and boost the signal, we weight the redshift bins by their galaxy count and combine them. Following Greco et al. (2018); Greene et al. (2022), we expect the LSBGs to live at low redshifts, thus the lensing efficiency varies little between the assorted redshift bins. Furthermore, combining the source bins at the measurement level circumvents the need to measure the cross-covariance between redshift bins. We display the combined redshift distribution in Fig. 1 and determine a mean source redshift of 0.6312.

2.3 2Mass Photometric Redshift Catalog

Following the work of Giannini et al. (2022), we use the clustering redshifts method to obtain a rough estimate of the LSBG redshift distribution. We cross-correlate the positions of the LSBG catalog with the positions of the 2Mass Photometric Redshift Catalog (2MPZ) (Bilicki et al. 2014), which contains approximately 10^6 galaxies. The catalog cross-matches the 2MASS Extended Source Catalog, WISE, and SuperCosmos samples and utilizes the artificial neural network approach (the ANNz algorithm) (Collister & Lahav 2004) to derive the photometric redshifts (Jarrett et al. 2000; Hambly et al. 2001; Kovacs et al. 2013) of the sampled galaxies.

3 MEASUREMENT

3.1 Tangential Shear Measurements

Galaxy-galaxy lensing traces mass distributions by cross-correlating the shapes of background (source) galaxies with the positions of foreground galaxies. We first measure the ellipticity of the source galaxies to extract the cosmic shear, γ. The lensing distortion orients the source image tangentially around the lens image. For a particular lens-source galaxy pair (LS), we find the tangential component of the ellipticity:

$$e_{t,LS} = -e_1 \cos(2\phi) - e_2 \sin(2\phi). \quad (4)$$

We define ϕ as the position angle of the source galaxy centered at the lens galaxy with respect to the x-axis of the sky coordinate system, and e_1 and e_2 as the ellipticity components.

Assuming the galaxies are randomly oriented, averaging the tangential component of the ellipticity over many source-lens pairs reduces their intrinsic shape. We can obtain the tangential shear:

$$\gamma_t(\theta) = \frac{\Sigma_{LS} w_{LS} e_{t,LS}(\theta)}{\Sigma_{LS} w_{LS}(\theta)}, \quad (5)$$

with $w_{LS} = (w_L)(w_S)$ as the weight factor for a particular lens-source pair, w_L as the weight of the lens galaxy, w_S as the weight of the source galaxy, and θ as the angular distance between the lens and the source galaxy pair. The lens galaxy weights are uniform with $w_L = 1$.

We must correct the tangential shear measurements by incorporating random point subtraction and the shear response. Random point subtraction requires measuring the tangential shear around a sample of random points to test the edges of the survey and masked regions for systematics. The sample of random points comes from the Y3 Gold Footprint catalog (Sevilla-Noarbe et al. 2021). The shear estimator with random point subtraction is given by

$$\gamma_t(\theta) = \frac{\Sigma_{LS} w_{LS} e_{t,LS}(\theta)}{\Sigma_{LS} w_{LS}(\theta)} - \frac{\Sigma_{RS} w_{RS} e_{t,RS}(\theta)}{\Sigma_{RS} w_{RS}(\theta)}. \quad (6)$$

The response factor corrects the mean tangential shear and eliminates biases caused by noisy ellipticity measurements or selections.

	$\chi^2_{\rm null}/\nu$	S/N
Full Sample	50.09/22	5.30
Red	66.42/22	6.67
Blue	26.70/22	2.17

Table 1: Signal-to-noise and χ^2 values for tangential shear measurements of red, blue, and total LSBG samples. ν represents degrees of freedom.

We find the response factor for the combined source redshift bins to be 0.7184. We list the tangential shear estimator with the incorporated response factor as follows:

$$\gamma_t(\theta) = \frac{1}{\langle R \rangle}\left[\frac{\Sigma_{LS} w_{LS} e_{t,LS}(\theta)}{\Sigma_{LS} w_{LS}(\theta)} - \frac{\Sigma_{RS} w_{RS} e_{t,RS}(\theta)}{\Sigma_{RS} w_{RS}(\theta)}\right]. \quad (7)$$

3.2 Tangential Shear Measurement Pipeline

We perform the lensing measurements with the software package TreeCorr (Jarvis et al. 2004). We use the NGCorrelation class from TreeCorr to complete the position-shape correlations. TreeCorr splits the lens galaxies and random points into 100 patches to obtain the jackknife covariance. Based on the survey area (5000 deg^2), the maximum length of the jackknife patches is $\sim$ 400 arcmin, establishing the upper bound of the measurement scales. As such, we execute the measurements in 22 angular bins spanned logarithmically from 0.25 to 400 arcmin. We display the tangential shear measurements in Fig. 2 and the jackknife correlation matrices in Fig. 3.

We evaluate the χ^2 of the measurements by combining the inverse covariance with the measurement signal:

$$\chi^2 = (\gamma_{t_d} - \gamma_{t_m})\mathrm{cov}^{-1}(\gamma_{t_d} - \gamma_{t_m}). \quad (8)$$

We define γ_{t_d} as the measured tangential shear and γ_{t_m} as the modeled shear. We compare the tangential shear measurements to a null model to assess the strength of the lensing signal. We use the Hartlap factor (Hartlap et al. 2007) to correct for the noise and bias of the inverse jackknife covariance. The Hartlap factor scales the inverse of the covariance matrix by

$$f = (n - m - 2)/(n - 1), \quad (9)$$

with n as the number of realizations (100) and m as the number of entries in the data vectors (22). We evaluate the signal-to-noise,

$$\mathrm{S/N} = \sqrt{\chi^2_{\rm null} - \nu}, \quad (10)$$

where ν corresponds to the number of degrees of freedom (22).The signal-to-noise and $\chi^2_{\rm null}$ values are listed in Table 1. Despite containing fewer galaxies than the total sample, the red LSBG population produces the strongest shear signal, likely due to the clustered environments of these galaxies.

3.3 Tangential Shear Measurement Validation

3.3.1 $\gamma_\times$ Shear

We compute the $\gamma_\times$ term as a systematics test on the tangential shear measurements. While the γ_t term measures the shear of the lensing E-mode, the $\gamma_\times$ term measures the shear of the lensing B-mode. Weak lensing only produces a tangential shear, thus in the absence of systematics the $\gamma_\times$ term must remain consistent with zero, as shown in Fig. 4. We measure a $\chi^2_{\rm null}$ for the $\gamma_\times$ term of 13.58/22 for the total sample, 14.84/22 for the red sample, and 15.96/22 for the blue sample.

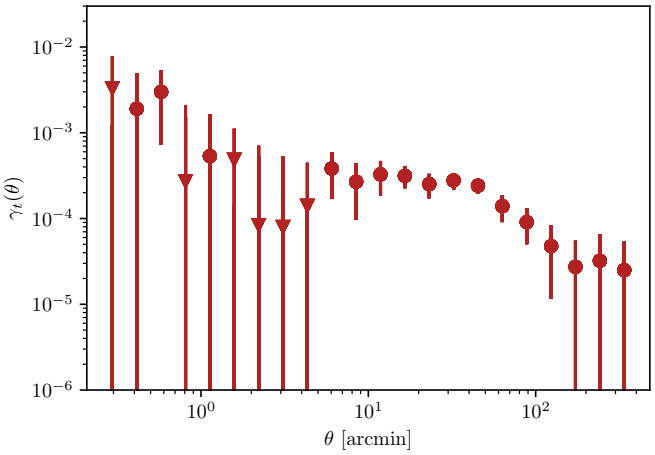

(a) Red LSBGs

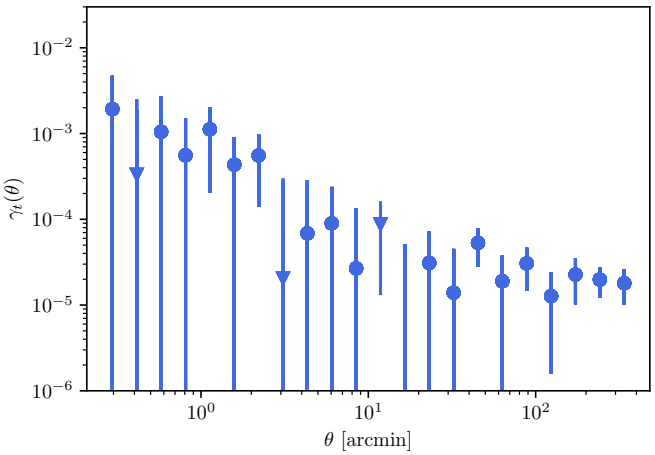

(b) Blue LSBGs

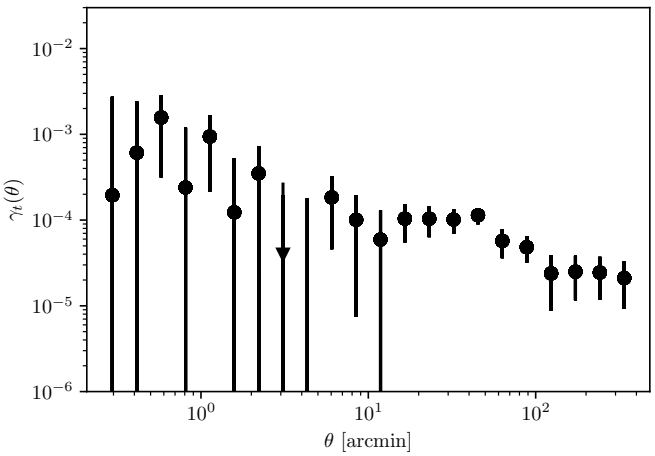

(c) Total LSBG Sample

Figure 2. Tangential shear measurements for the red, blue, and total sample of LSBGs. The measurements span from 0.25-400 arcmin and are divided into 22 angular bins. The triangle markings indicate bins with negative shear measurements. The errorbars are derived from the jackknife covariance.

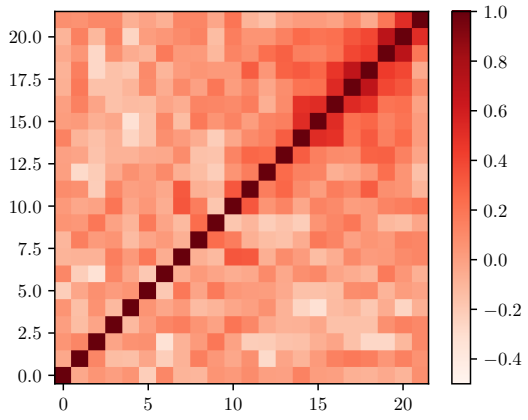

(a) Red LSBGS

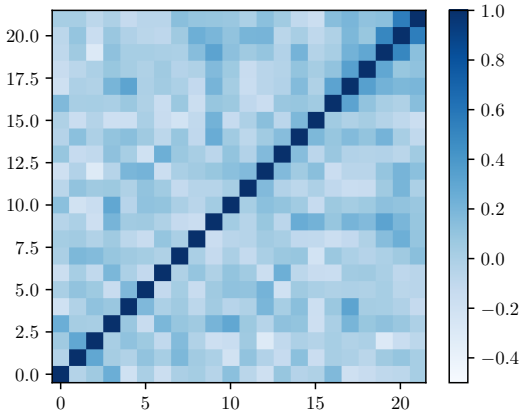

(b) Blue LSBGs

Figure 3. Correlation matrices for the jackknife covariance of red and blue LSBGs. The x and y axes correspond to the angular bins of the tangential shear measurements. At larger scales (bins>14), the correlation between bins grows stronger.

3.3.2 Random Sample Shear

As an additional test, we measure the tangential shear surrounding the positions of the randoms catalog. These positions are randomly selected, therefore we should not measure any lensing signal. We find a $\chi^2_{\rm null}$ of 3.21 over 22 degrees of freedom, confirming a null signal. We illustrate this result in Fig. 5.

3.4 Interpreting Red LSBG Tangential Shear Measurements

As described in Tanoglidis et al. (2021) and shown in fig VIII, the red LSBG sample demonstrates a preference for clustered environments. Theoretical modeling indicates that faint, clustered, red galaxies are predominantly satellites of massive dark matter halos. Berlind et al. (2005) used a high resolution, small-volume simulation to demonstrate that low-luminosity red galaxies primarily live as satellites in massive halos. Zehavi et al. (2011) found that the strong clustering exhibited by faint red galaxies suggested that most of these galaxies are satellites in massive halos. The fainter the galaxy population, the greater the satellite fraction. Given these concurring results, we assume the red LSBG sample is dominated by satellites.

Based on its scattered spatial distribution, the blue LSBG sample is likely composed of central field galaxies. This behavior reduces the

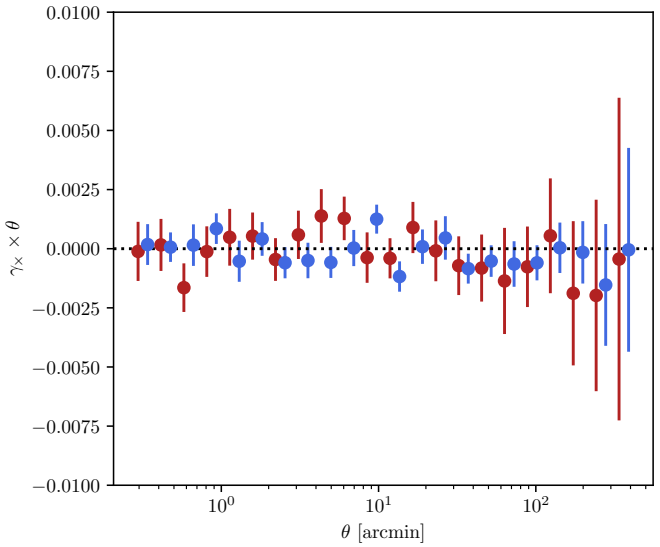

Figure 4. Measurement of the $\gamma_\times$ term for the red and blue LSBG samples. Note that the blue sample positions are offset to improve visibility. We find this term to be consistent with zero.

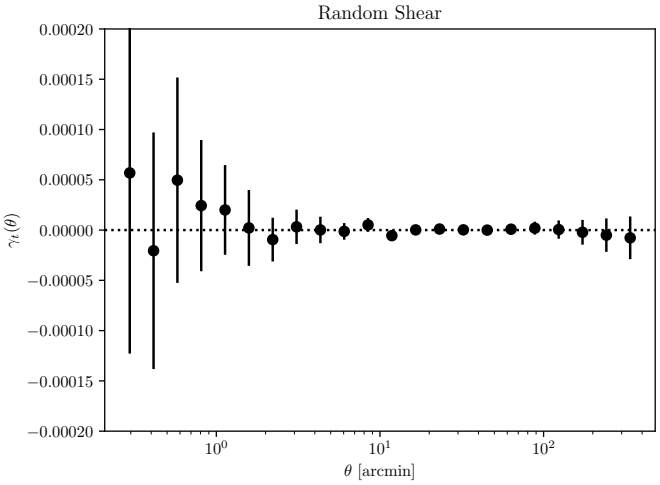

Figure 5. Tangential shear measurements around the random point sample, divided into 22 angular bins. All shape catalog redshift bins are combined. The shear measurements do not produce a significant signal, with a $\chi^2_{\rm null}$ of 3.21/22.

lensing signal and hinders our ability to obtain an effective redshift distribution to model the blue LSBGs. Given these complications, we focus our efforts on modeling the red LSBG sample.

3.5 Deriving the Redshift Distribution

The two-point correlation signal measures the likelihood of finding a pair of objects at a given separation compared to a random distribution. In other words, it is a gauge of clustering. Clustering-based redshift methods derive the redshift distribution of an "unknown" galaxy sample by exploiting the two-point correlation signal between the "unknown" sample and a "reference" sample of galaxies with trusted redshifts divided into thin bins. We define the "unknown" sample as the red LSBG catalog and the "reference" sample as the 2MPZ catalog (Bilicki et al. 2014). This process assumes that the cross-correlation between the two samples is positive when the objects overlap in physical space. We compute the cross-correlation signal as a function of angular scale by using the Davis & Peebles (1983) estimator:

$$w_{ur}(\theta) = \frac{N_{Rr}}{N_{Dr}} \frac{D_u D_r(\theta)}{D_u R_r(\theta)} - 1. \tag{11}$$

w_{ur} represents the cross-correlation signal between the unknown and reference sample, $D_u D_r(\theta)$ and $D_u R_r(\theta)$ stand for the data-data and data-random pairs, and N_{Rr} and N_{Dr} correspond to the total number of galaxies in the reference sample and the reference random catalog, used for normalization. We use the TreeCorr NNCorrelation class to evaluate the position-position correlations. We show the cross-correlation measurements across angular scales in Fig. 6 and observe a positive measurement, indicating redshift overlap between the catalogs. We average the correlation function over specified angular scales via

$$\bar{w}_{ur} = \int_{\theta_{\min}}^{\theta_{\max}} W(\theta) w_{ur}(\theta) d\theta, \tag{12}$$

where we use $W(\theta) \propto \theta^{-1}$ as a weighting function to yield optimal S/N in the presence of shot noise. Given the low redshift range of the LSBG sample implied by Tanoglidis et al. (2021), we divide the reference sample into thin redshift bins with a width of 0.01 over the range [0.0-0.14]. We approximate the redshift distribution at the central redshift of each bin z_i as

$$n_u(z_i) \propto \frac{w_{ur}(z_i)}{b_r(z_i) w_{DM}(z_i)}. \tag{13}$$

$b_r(z_i)$ signifies the galaxy-matter bias of the reference sample. We estimate $b_r(z)$ by measuring the angle-averaged auto-correlation function of the reference sample:

$$b_r(z_i) \approx \sqrt{\frac{w_{rr}(z_i)}{w_{DM}(z_i)}}. \tag{14}$$

We use CosmoSIS, a state-of-the-art cosmological parameter sampler, to recover $W_{DM}(z_i)$, the dark matter two-point correlation function for the specified redshift bins. The galaxy bias appears most linear at the angular scales of θ = 16.53 arcmin, θ = 23.13 arcmin, θ = 32.45 arcmin, θ = 45.23 arcmin, and θ = 63.25 arcmin. For confirmation, we plot the galaxy bias as a function of angular scale in Appendix B. We extract the redshift distribution over these angular scales and show the resulting distributions in Fig. 7. We average these distributions to produce a final approximated redshift distribution for the LSBG sample, found in Fig. 8. As an additional point of interest, we cross-correlate the red LSBG sample with the Magnitude-Limited

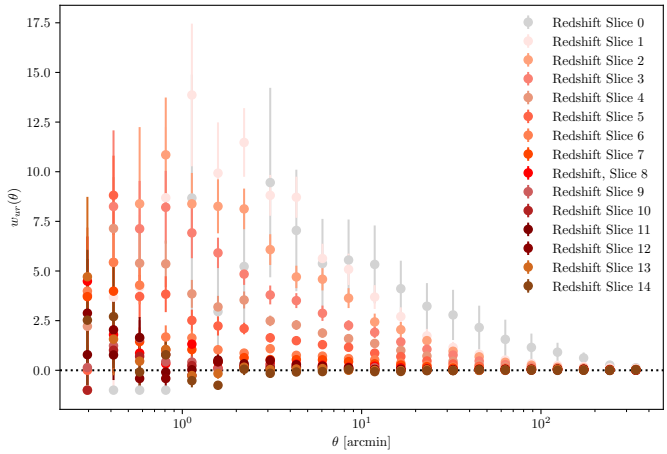

Figure 6. Cross-correlation between the red LSBG positions and the 2MPZ catalog across angular scales, in 14 redshift slices spanning from 0.0 to 0.14 with a width of 0.01

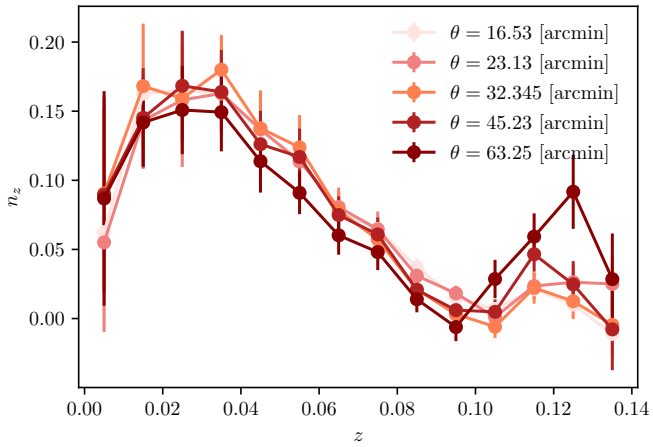

Figure 7. Normalized redshift distribution of the red LSBGs for angular scales of θ = 23.13[arcmin], θ = 32.345[arcmin] and θ = 45.23[arcmin]. The uncertainties on the autocorrelation and cross-correlation functions, obtained using the jackknife covariance, are propagated forward to produce the errorbars.

Lens Sample (MagLim) (Porredon et al. 2022) and the redMaGiC sample (Pandey et al. 2022), described in Appendix A. We present the cross-correlation measurements for the blue LSBG sample in Appendix A3.

4 MODELING THE TANGENTIAL SHEAR

We denote the tangential shear for a single lens-source system as

$$\gamma_{t,i,j}(R) = \frac{\Delta\Sigma_i(R)}{\Sigma_{\rm crit}(z_{L,i}, z_{S,j})}, \tag{15}$$

where i and j represent the indices for a single lens and source object, and $\Delta\Sigma(R)$ describes the excess surface density as a function of the projected radius R, the physical distance between the lens and the source galaxy at the lens redshift. $\Sigma_{\rm crit}(z_L, z_S)$ describes a geometrical factor dependent on the characteristics of the lensing

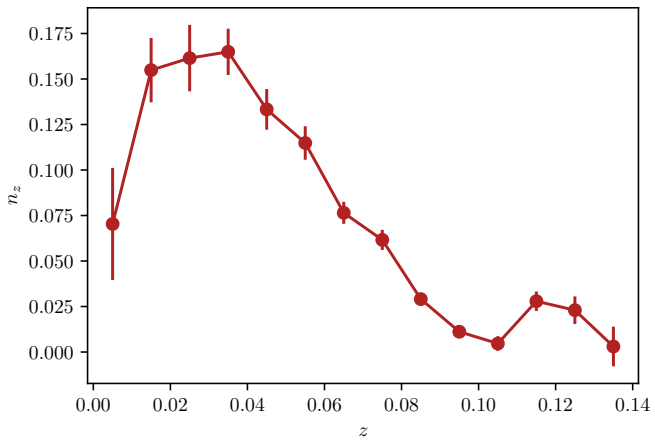

Figure 8. Normalized redshift distribution of the red LSBGs averaged over the angular scales of θ = 23.13[arcmin], θ = 32.345[arcmin] and θ = 45.23[arcmin].

system, given by

$$\Sigma_{\rm crit}(z_L, z_S) = \frac{c^2}{4\pi G}\frac{D_S}{D_{LS}D_L}, \tag{16}$$

where c represents the speed of light and D_S, D_L, and D_{LS} stand for the angular diameter distances to the source, the lens, and between the source and the lens. The angular diameter distances can be determined from the redshifts and the cosmology.

4.1 Excess Surface Density

The excess surface density can be broken into two components:

$$\Delta\Sigma(R) = \Sigma(< R) - \Sigma(R), \tag{17}$$

where $\Sigma(R)$ designates the projected surface density at R and $\Sigma(< R)$ represents the cumulative surface density within the projected radius R. Given their dependence on R, both terms implicitly rely on the lens redshift. We define the cumulative surface density as

$$\Sigma(< R) = \frac{2}{R^2}\int_0^R r\Sigma(r)dr, \tag{18}$$

where r stands for the varying physical radius. We describe the projected surface density as

$$\Sigma(R) = 2\int_0^{+\infty} \rho_{\rm NFW}(\sqrt{r^2 + R^2})dr. \tag{19}$$

$\rho_{\rm NFW}$ signifies a Navarro-Frank-White (NFW) profile (Navarro et al. 1996). The NFW profile describes the density of dark matter as a function of the distance from the center of a galaxy or cluster. The density at a radius r is given by

$$\rho_{\rm NFW}(r) = \frac{\rho_s}{r/r_s(1 + r/r_s)^2}, \tag{20}$$

where r_s stands for the scale radius. We write the scale radius as

$$r_s = \frac{r_{200}}{c_s}, \tag{21}$$

where c_s denotes the concentration of the halo and r_{200} signifies the virial radius. ρ_s stands for the characteristic density of the halo. The characteristic density represents the density of the dark matter halo within the scale radius r_s and can be derived from the mass and the concentration via

$$\rho_s = \frac{M_{\rm halo}}{4\pi r_s^3(\ln(1 + c_s) - c_s/(1 + c_s))}, \tag{22}$$

where $M_{\rm halo}$ stands for the effective halo mass of the sample, or the average of the halo mass function for the LSBG halos. The NFW profile acts as a mediator between the halo mass and the excess surface density.

4.2 Tangential Shear for a Galaxy Population

We integrate over the redshift distributions to construct a tangential shear model with a range of possible source and lens redshifts:

$$\gamma_{t,\rm pop}(R) = \int\int(\gamma_{t,i,j}(R) \times N(z_S) \times N(z_L))dz_S dz_L, \tag{23}$$

where $N(z_L)$ and $N(z_S)$ represent the normalized redshift distributions for the lenses and sources and $\gamma_{t,i,j}$ corresponds to the tangential shear profiles for the individual systems.

The shear model consists of a stellar term, signifying the LSBG stellar mass, a subhalo term, derived from the LSBG subhalo mass, and a host halo term, representing the influence of the LSBG host halo. The stellar portion takes precedence at unobservable small scales and does not contribute significantly to the measured lensing signal. The dark matter distribution of a satellite galaxy is centered on the subhalo. Consequently, the subhalo term leads at smaller angular separations and the host halo term dominates at larger angular separations. For the host halo model, we must incorporate a radial offset to shift the reference point from the projected center of the profile. We feed the radial offset into an offset excess surface density profile:

$$\Sigma_{\rm off}(R, R_{\rm off}) = \frac{1}{2\pi}\int_0^{2\pi}\Sigma(\sqrt{R_{\rm off}^2 + R^2 + 2RR_{\rm off}\cos\theta})d\theta, \tag{24}$$

where $R_{\rm off}$ represents the projected physical distance between the new reference and the center of the profile, and θ signifies a range between 0 and 2π to calculate the angular integral. We define the host halo shear model with the offset excess surface density profile as

$$\gamma_{t,\rm host} = \frac{\Delta\Sigma(R, R_{\rm off})}{\Sigma_{\rm crit}(z_L, z_S)}. \tag{25}$$

The tangential shear model for a subhalo and an offset host halo can be written as

$$\gamma_t(R) = \gamma_{t,\rm sub}(R) + \gamma_{t,\rm host}(R, R_{\rm off}). \tag{26}$$

4.3 Modeling Pipeline

We employ Profiley, a Python-based package that generates mass distribution profiles for galaxies, to construct NFW profiles dependent on a given redshift, concentration, and mass (Madhavacheril et al. 2020). We define the concentration by applying the Ishiyama et al. (2021) concentration-mass relationship and implement the 'Planck15' cosmology, a ΛCDM model with values of Ω_{m0} = 0.3809, Ω_{de0} = 0.6910, and Ω_{b0} = 0.0486 (Planck Collaboration 2016).

We use a specified lens redshift to convert the tangential shear measurements from angular to physical scales:

$$R = D_L \times \theta. \tag{27}$$

D_L stands for the angular diameter distance (based on the given

lens redshift and the cosmology) and θ represents the angular scales. Profiley uses these converted physical radii and the established NFW profile to produce the excess surface density with the `nfw.projected_excess` function. The lens and source redshift can be used to construct the $\Sigma_{\rm crit}(z_L, z_S)$ term with the `nfw.sigma_crit` function. We follow Eq. 15 to generate the shear profile for a single lens and source redshift.

We utilize the lens redshift distribution of Sec. 3.5. We find that using a single fixed source redshift versus the full distribution of source redshifts does not significantly impact the model, inducing a $\Delta\chi^2$ of only 0.12. We fix the source redshift at the mean redshift of 0.6312 and only integrate $\gamma_{t,i,j}$ over the lens redshift distribution,

$$\gamma_{t,\rm sub,pop}(R) = \int \gamma_{t,i,j}(R) \times N(z_L) dz_L. \tag{28}$$

This equation represents the subhalo term of the total model.

We determine the necessary radial offset for the host halo profile. Upon examination, the shape of the red LSBG tangential shear measurements changes at $\sim$ 40 arcmin. Assuming the red LSBGs are satellite galaxies at low redshift, this angular separation corresponds to a physical radius consistent with the onset of the host halo profile (Zacharegkas et al. 2022).

Following the same procedure as the subhalo model, we initialize a new, separate NFW profile for the host halo based on a given lens redshift, concentration, and mass. We convert the angular scales of the central offset, defined as μ, to physical scales using the selected lens redshift and Eq. 27. To represent the host halos of a galaxy population with various offset radii, we build a normal distribution of radial offsets centered around μ with a σ of $\frac{\mu}{3}$, spanning from 0 to $2 \times \mu$. We illustrate that this distribution width suits the data in Fig. C2. We use the Profiley `nfw.offsetprojected_excess` function to produce the offset excess surface density profile and divide by $\Sigma_{\rm crit}(z_L, z_S)$, following Eq. 25. We integrate over both the offset distribution and the lens redshift distribution, defining the host halo model as

$$\gamma_{t,\rm host,pop}(R, R_{\rm off}) = \int\int \gamma_{t,i,j}(R, R_{off}) \times N(R_{\rm off}) \times N(z_L) dR_{\rm off} dz_L. \tag{29}$$

5 FITTING THE MODEL

We fit the model to the tangential shear measurements with a Markov Chain Monte Carlo, or MCMC. An MCMC is a statistical sampling algorithm that utilizes the likelihood function to estimate the posterior distribution of model parameters given some observed data. To avoid numerical complications, we use the logarithm of the likelihood function, defined as

$$\ln(L) = \frac{-1}{2}(\gamma_{t,d} - \gamma_{t,m}(\mathbf{p}))\mathrm{cov}^{-1}(\gamma_{t_d} - \gamma_{t,m}(\mathbf{p})), \tag{30}$$

with $\gamma_{t,d}$ established as the tangential shear measurement, and $\gamma_{t,m}$ set as the modeled shear, constructed from the chosen parameters. The *Bayes theorem* transforms the likelihood function into $P(\mathbf{p}|\mathbf{d})$, or the probability that the parameters $\mathbf{p}$ take on certain values given a set of measurements $\mathbf{d}$,

$$P(\mathbf{p}|\mathbf{d}) = \frac{P(\mathbf{d}|\mathbf{p}) \times P(\mathbf{p})}{P(\mathbf{d})} \propto L(\mathbf{p}) P(\mathbf{p}), \tag{31}$$

where $P(\mathbf{p})$ represents the prior. The prior folds any previous knowledge of the parameters $\mathbf{p}$ into the analysis to define the bounds of the MCMC. We select the free parameters of the model,

$$\mathbf{p} = (M_{\rm host}, M_{\rm sub}, \mu). \tag{32}$$

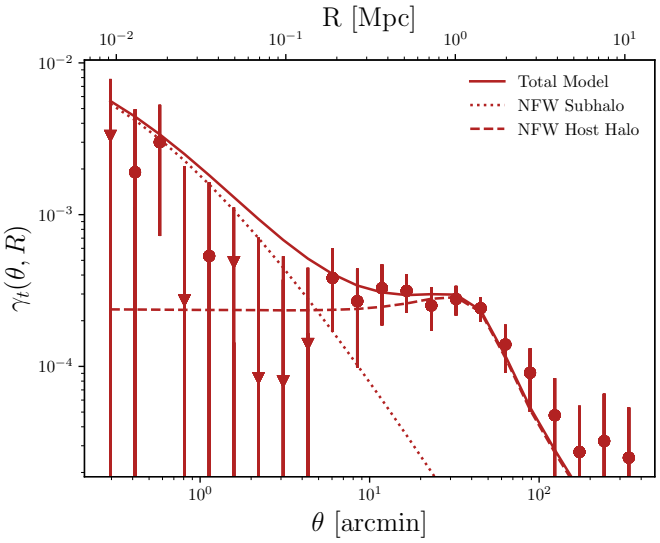

Figure 9. Total model fit to the red galaxy tangential shear measurements. With the given MCMC parameter values of Table 2 for the host halo mass, subhalo mass, and offset, we find a χ^2 value of 33.27 over 22 degrees of freedom between the model and the measurements. Note that the triangle markers indicate a negative shear measurement.

$P(\mathbf{p}|\mathbf{d})$ signifies the posterior distribution. These posteriors correspond to the maximum probability of measurements, assuming that the model is effective. We use the algorithm emcee to generate the MCMC, with 1000 steps and 20 walkers (Goodman & Weare 2010).

5.1 Priors

We apply uniform priors to the subhalo mass, host halo mass, and offsets, with the following ranges: $10^7 M_\odot < M_{\rm sub} < 10^{12} M_\odot$, $10^{10} M_\odot < M_{\rm host} < 10^{15} M_\odot$, 25 arcmin $< \mu <$ 55 arcmin.

5.2 Posteriors

We rely on ChainConsumer to calculate the mean of the posteriors (Hinton 2016). We find the MCMC converges at an offset of $38.7^{+4.7}_{-4.6}$ arcmin and a host halo mass of $7.3^{+2.0}_{-1.6} \times 10^{12} M_\odot$. We find an upper bound for the subhalo mass at $2.8 \times 10^{11} M_\odot$. These values are listed in Table 2 and shown in Fig. 10. We use these posteriors to build the model displayed in Fig. 9. These results are consistent with Sifón et al. (2018); Prole et al. (2019); van Dokkum et al. (2016).

6 STELLAR TO HALO MASS RELATION

6.1 Stellar Mass

We draw on the lens sample photometry and the lens redshift distribution of Sec. 3.5 to estimate the stellar mass of the red LSBG sample. The ratio between the stellar mass and the subhalo mass (M_*/M_h) can be compared to the satellite-specific parameterized stellar-to-halo-mass relation (Moster et al. 2010). We adopt the method developed in Bell et al. (2003) to extract the mass-to-light ratio from the photometry, the so-called color-to-mass-light relation (CMLR):

$$\log \gamma^j_* = a_j + b_j \times \mathrm{color}. \tag{33}$$

Red Galaxies	Priors	Posteriors
Subhalo Mass	$U(10^7 M_\odot < M_{\rm sub} < 10^{12} M_\odot)$	$M_{\rm sub} < 2.8 \times 10^{11} M_\odot$
Host Halo Mass	$U(10^{10} M_\odot < M_{\rm host} < 10^{15} M_\odot)$	$7.3^{+2.0}_{-1.6} \times 10^{12} M_\odot$
Offset	U(25 arcmin $< \mu <$ 55 arcmin	$38.7^{+4.7}_{-4.6}$ arcmin

Table 2: Priors and posteriors for the red LSBG tangential shear measurements for the subhalo mass, host halo mass, and mean radial offset given by the MCMC, corresponding to Fig. 10. We define $U(a < x < b)$ as a uniform distribution with a lower bound of a and an upper bound of b. Note that the subhalo mass posterior is unconstrained at the low mass end. We list the 95% upper bound.

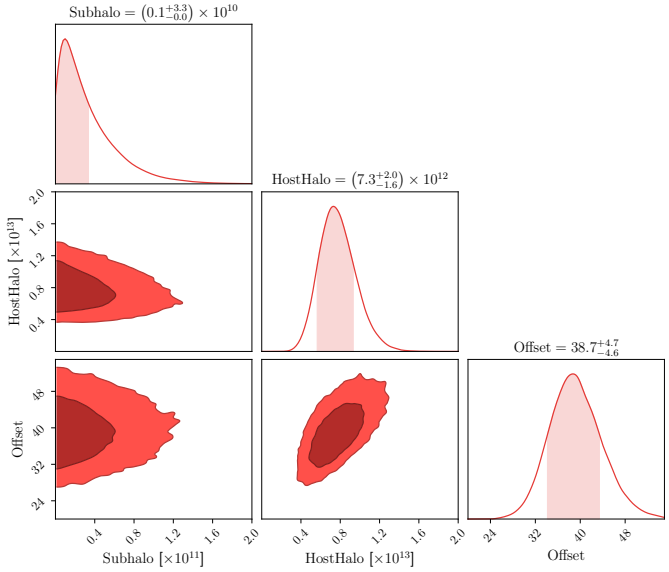

Figure 10. MCMC posterior distribution for red LSBGs.

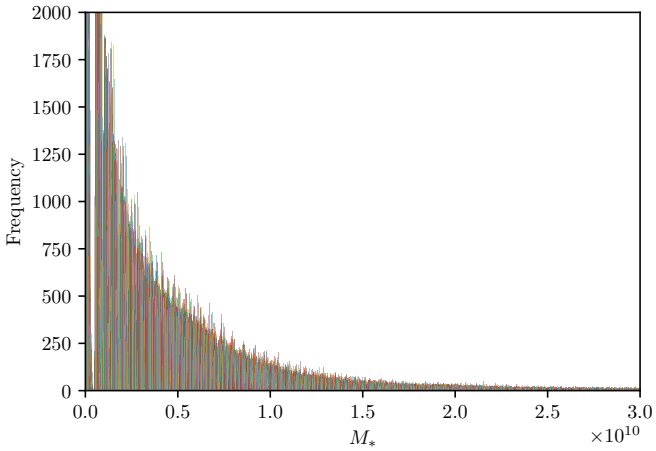

Figure 11. Distribution of stellar masses for the red LSBG sample, approximated using the i-band, g-band, and r-band photometry and the $g-i$ and $g-r$ color bands. The stellar mass distribution is resampled around the uncertainty of the magnitudes.

Color	a_g	b_g	a_r	b_r	a_i	b_i
$g-r$	-0.499	1.519	-0.306	1.097	-0.222	0.864
$g-i$	-0.379	0.914	-0.220	0.661	-0.152	0.518

Table 3: Zero-point and slope parameters for the CMLR (Bell et al. 2003) for the g-band, i-band, and r-band magnitudes and the $g-r$ and $g-i$ colors.

γ_*^j represents the stellar mass-to-light ratio, j stands for the selected band, a_j indicates the zero-point of the function, and b_j signifies the slope of the function. As described in Du et al. (2020), the $g-r$ and the $g-i$ bands prove to be the most robust indicators of γ_*. We define the parameter values from Bell et al. (2003) in Tab. 3. We compare the impact of various magnitude band and color choices on the stellar mass estimate in Fig. 11.

We extract the lens sample luminosity in the j-band from the photometry and combine it with the mass-to-light ratio to estimate the stellar mass. We calculate the comoving distance to the established lens redshift distribution from Sec. 3.5 with the 'Planck15' cosmology. We utilize the distance modulus to find the absolute j-band magnitude of the lens sample:

$$m_j - M_j = 5 \log\left(\frac{d}{10\text{pc}}\right). \tag{34}$$

M_j represents the absolute j-band magnitude of the lens sample, m_j stands for the apparent magnitude in the j-band, and d indicates the comoving distance to the lens sample (converted to parsecs). We compare the LSBG absolute magnitude to the solar absolute magnitude to recover the luminosity:

$$\frac{L_j}{L_\odot} = 10^{0.4(M_{j,\odot} - M_j)}. \tag{35}$$

$M_{j,\odot}$ represents the absolute magnitude of the sun in the j-band for the AB magnitude SDSS filter. We multiply the luminosity by the mass-to-light ratio to find the stellar mass:

$$M_* = L_j \times \gamma_*^j. \tag{36}$$

We resample the stellar mass distribution around the uncertainty of the j-band magnitudes, as shown in Fig. 11. We conduct this mass estimate for the g-band, r-band, and i-band magnitudes and the $g-i$ and $g-r$ colors. The stellar mass distribution is consistent with the stellar mass distribution of satellite galaxies in the SAGA survey (Mao et al. 2021).

6.2 Stellar to Halo Mass Relation

We compare the ratio between the stellar mass estimates and the constrained red galaxy subhalo mass from Sec. 5.2 to the satellite-specific parameterized SHMR. We adopt the power law definition of the stellar-to-halo mass relation from Moster et al. (2010):

$$\frac{M_\star}{M_h}(z) = 2A(z) \left[\left(\frac{M_h}{M_A(z)}\right)^{-\beta(z)} + \left(\frac{M_h}{M_A(z)}\right)^{\gamma(z)} \right]^{-1}. \tag{37}$$

$M_\star$ represents the stellar mass, M_h designates the halo mass, $A(z)$ indicates the normalization of the SHMR at the characteristic halo mass M_A, and β and γ describe the slopes of the relation at low- and high-mass ends. We employ the best-fit parameters for low-redshift satellite galaxies found in Moster et al. (2010):

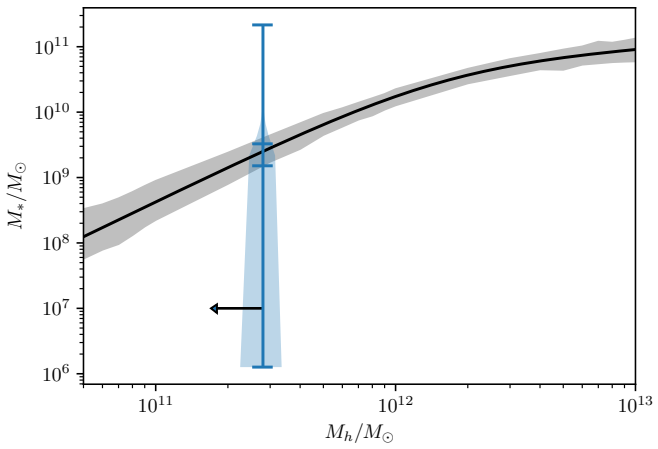

Figure 12. Comparison between the the LSBG stellar mass (M_*) calculated for the i-band magnitude and $g-i$ color at the upper subhalo mass limit and the stellar mass estimated with the parameterized SHMR by Moster et al. (2010). The markings indicate the mean, median, and the extrema of the stellar mass distribution. The shaded grey areas represent the spread of the stellar mass estimate obtained from the SHMR.

$A = 0.0186^{+0.0012}_{-0.0012}$, $\log M_A = 12.1988^{+0.0878}_{-0.0878}$, $\beta = 0.7817^{+0.0629}_{-0.0629}$, and $\gamma = 0.7334^{+0.0452}_{-0.0452}$. We depict the spread of the i-band and $g-i$ LSBG stellar mass estimate at the upper subhalo mass limit as an illustrative example and compare to the stellar mass distribution obtained with the parameterized satellite SHMR in Fig. 12.

7 CONCLUSIONS

We perform galaxy-galaxy lensing measurements on a sample of low-surface-brightness galaxies from Tanoglidis et al. (2021). We use the DES Y3 Metacalibration catalog for the source galaxy shapes. We divide the lens sample into two subcategories: red galaxies with $g-i > 0.6$ and blue galaxies with $g-i < 0.6$. We measure the tangential shear around the lens galaxies across angular scales of 0.25-400 arcmin and extract a signal-to-noise of 6.67 for red galaxies, 2.17 for blue galaxies, and 5.30 for the combined sample.

We cross-correlate the positions of the red LSBGs with the 2MPZ catalog to extract the redshift distribution of the red LSBG sample. We construct a model built out of two NFW profiles to represent the subhalo and host halo terms of the red LSBG sample. We fit the model to the red LSBG measurements with an MCMC to recover posterior values for the subhalo mass, host halo mass, and mean radial offset of the host halo. We obtain an upper bound on the subhalo mass with 95% certainty at $2.8 \times 10^{11} M_\odot$. We estimate the host halo mass at $7.3^{+2.0}_{-1.6} \times 10^{12} M_\odot$ and the radial offset at $38.7^{+4.7}_{-4.6}$ arcmin, with a fixed source redshift of 0.6312. These results are presented in Table 2.

We use the lens photometry to estimate the stellar mass of the red LSBG sample by adopting the color-mass light relation of Bell et al. (2003). We combine the stellar mass estimate with the subhalo mass posterior to obtain the LSBG stellar-to-halo mass ratio. We compare this measurement to the parameterized satellite stellar-to-halo mass relation of Moster et al. (2010). This project represents the first attempt to constrain the mass range of LSBGs using weak gravitational lensing.

ACKNOWLEDGMENTS

Funding for the DES Projects has been provided by the U.S. Department of Energy, the U.S. National Science Foundation, the Ministry of Science and Education of Spain, the Science and Technology Facilities Council of the United Kingdom, the Higher Education Funding Council for England, the National Center for Supercomputing Applications at the University of Illinois at Urbana-Champaign, the Kavli Institute of Cosmological Physics at the University of Chicago, the Center for Cosmology and Astro-Particle Physics at the Ohio State University, the Mitchell Institute for Fundamental Physics and Astronomy at Texas A&M University, Financiadora de Estudos e Projetos, Fundação Carlos Chagas Filho de Amparo à Pesquisa do Estado do Rio de Janeiro, Conselho Nacional de Desenvolvimento Científico e Tecnológico and the Ministério da Ciência, Tecnologia e Inovação, the Deutsche Forschungsgemeinschaft and the Collaborating Institutions in the Dark Energy Survey.

The Collaborating Institutions are Argonne National Laboratory, the University of California at Santa Cruz, the University of Cambridge, Centro de Investigaciones Energéticas, Medioambientales y Tecnológicas-Madrid, the University of Chicago, University College London, the DES-Brazil Consortium, the University of Edinburgh, the Eidgenössische Technische Hochschule (ETH) Zürich, Fermi National Accelerator Laboratory, the University of Illinois at Urbana-Champaign, the Institut de Ciències de l'Espai (IEEC/CSIC), the Institut de Física d'Altes Energies, Lawrence Berkeley National Laboratory, the Ludwig-Maximilians Universität München and the associated Excellence Cluster Universe, the University of Michigan, NSF's NOIRLab, the University of Nottingham, The Ohio State University, the University of Pennsylvania, the University of Portsmouth, SLAC National Accelerator Laboratory, Stanford University, the University of Sussex, Texas A&M University, and the OzDES Membership Consortium.

Based in part on observations at Cerro Tololo Inter-American Observatory at NSF's NOIRLab (NOIRLab Prop. ID 2012B-0001; PI: J. Frieman), which is managed by the Association of Universities for Research in Astronomy (AURA) under a cooperative agreement with the National Science Foundation.

The DES data management system is supported by the National Science Foundation under Grant Numbers AST-1138766 and AST-1536171. The DES participants from Spanish institutions are partially supported by MICINN under grants ESP2017-89838, PGC2018-094773, PGC2018-102021, SEV-2016-0588, SEV-2016-0597, and MDM-2015-0509, some of which include ERDF funds from the European Union. IFAE is partially funded by the CERCA program of the Generalitat de Catalunya. Research leading to these results has received funding from the European Research Council under the European Union's Seventh Framework Program (FP7/2007-2013) including ERC grant agreements 240672, 291329, and 306478. We acknowledge support from the Brazilian Instituto Nacional de Ciência e Tecnologia (INCT) do e-Universo (CNPq grant 465376/2014-2).

This manuscript has been authored by Fermi Research Alliance, LLC under Contract No. DE-AC02-07CH11359 with the U.S. Department of Energy, Office of Science, Office of High Energy Physics.

This work was supported in part by the U.S. Department of Energy, Office of Science, Office of Workforce Development for Teachers and Scientists (WDTS) under the Science Undergraduate Laboratory Internships Program (SULI).

REFERENCES

Bartelmann M., 2010, arXiv e-prints, p. arXiv:1010.3829
Bartelmann M., Maturi M., 2017, Scholarpedia, 12, 32440
Behroozi P. S., Conroy C., Wechsler R. H., 2010, ApJ, 717, 379
Bell E. F., et al. 2003, ApJS, 149, 289
Berlind A. A., et al. 2005, ApJ, 629, 625
Bernstein G. M., et al. 1995, AJ, 110, 1507
Bilicki M., et al. 2014, ApJS, 210, 9
Blanton M. R., et al. 2003, in American Astronomical Society Meeting Abstracts. p. 145.01
Bothun G., Impey C., McGaugh S., 1997, PASP, 109, 745
Cohen Y., et al. 2018, ApJ, 868, 96
Collister A. A., Lahav O., 2004, PASP, 116, 345
Danieli S., et al. 2017, ApJ, 837, 136
Das M., 2013, Journal of Astrophysics and Astronomy, 34, 19
Davis M., Peebles P. J. E., 1983, ApJ, 267, 465
Driver S. P., 1999, ApJ, 526, L69
Du W., et al. 2020, AJ, 159, 138
Gatti M., et al. 2021, MNRAS, 504, 4312
Giannini G., et al. 2022, arXiv e-prints, p. arXiv:2209.05853
Goodman J., Weare J., 2010, Communications in Applied Mathematics and Computational Science, 5, 65
Greco J. P., et al. 2018, ApJ, 857, 104
Greene J. E., et al. 2022, ApJ, 933, 150
Hambly N. C., et al. 2001, MNRAS, 326, 1279
Hartlap J., Simon P., Schneider P., 2007, A&A, 464, 399
Hayward C. C., Irwin J. A., Bregman J. N., 2005, ApJ, 635, 827
Hinton S. R., 2016, The Journal of Open Source Software, 1, 00045
Ishiyama T., et al. 2021, MNRAS, 506, 4210
Jarrett T. H., et al. 2000, AJ, 119, 2498
Jarvis M., Bernstein G., Jain B., 2004, MNRAS, 352, 338
Kado-Fong E., et al. 2021, ApJ, 920, 72
Kovacs A., et al. 2013, MNRAS, 431, L28
Leisman L., et al. 2017, ApJ, 842, 133
Madhavacheril M. S., et al. 2020, ApJ, 903, L13
Mao Y.-Y., et al. 2021, ApJ, 907, 85
Martin N. F., et al. 2013, ApJ, 776, 80
Martin G., et al. 2019, MNRAS, 485, 796
McConnachie A. W., 2012, AJ, 144, 4
McGaugh S. S., 1996, MNRAS, 280, 337
Minchin R. F., et al. 2004, MNRAS, 355, 1303
Moster B. P., et al. 2010, ApJ, 710, 903
Myles J., et al. 2021, MNRAS, 505, 4249
Navarro J. F., Frenk C. S., White S. D. M., 1996, ApJ, 462, 563
Niemiec A., et al. 2022, MNRAS, 512, 6021
O'Neil K., Bothun G., 2000, ApJ, 529, 811
Pandey S., et al. 2022, Phys. Rev. D, 106, 043520
Planck Collaboration 2016, A&A, 594, A13
Porredon A., et al. 2022, Phys. Rev. D, 106, 103530
Prat J., et al. 2022, Phys. Rev. D, 105, 083528
Prole D. J., et al. 2019, MNRAS, 484, 4865
Prole D. J., et al. 2021, MNRAS, 500, 2049
Rosenbaum S. D., et al. 2009, A&A, 504, 807
Sevilla-Noarbe I., et al. 2021, ApJS, 254, 24
Sifón C., et al. 2018, MNRAS, 473, 3747
Tanoglidis D., et al. 2021, ApJS, 252, 18
Thuruthipilly H., et al. 2023, arXiv e-prints, p. arXiv:2310.13543
Zacharegkas G., et al. 2022, MNRAS, 509, 3119
Zehavi I., et al. 2011, ApJ, 736, 59
van Dokkum P., et al. 2016, ApJ, 828, L6

APPENDIX A: FURTHER CROSS-CORRELATION MEASUREMENTS

In this appendix, we cross-correlate the LSBG samples with alternative catalogs. The MagLim and redMaGiC catalogs both have higher redshift cutoffs than the assumed maximum lens redshift of the LSBG distribution ($z > 0.20$ and $z > 0.15$, respectively). Based on this limit, we should not observe a positive cross-correlation signal. We find that the cross-correlation measurements are negative or null for both of these catalogs, cementing our assumption that these galaxies live at low redshifts.

For comparison, we also include the cross-correlation measurements between the blue LSBG sample and the 2MPZ catalog.

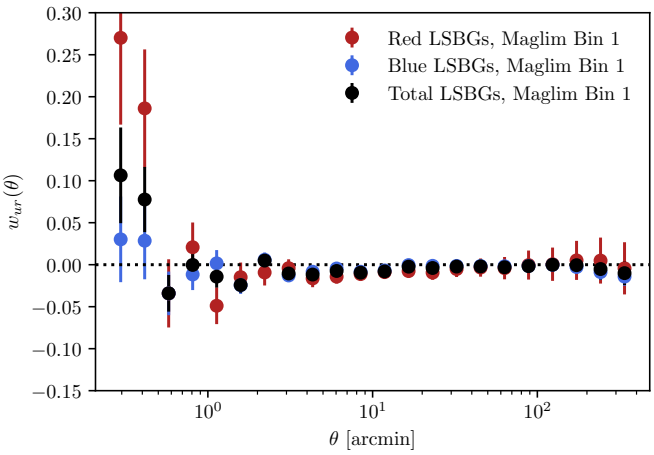

Figure A1. Cross-correlation between the first bin of the MagLim catalog and the red, blue and total LSBG samples.

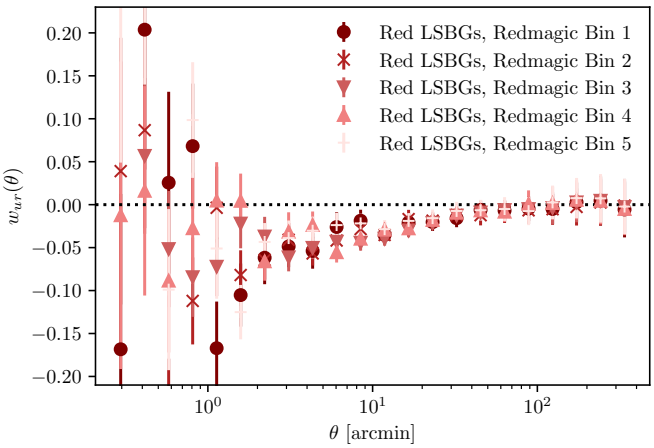

Figure A2. Cross-correlation between the five bins of the redMaGiC catalog and the red LSBG sample.

A1 MagLim Cross-Correlation

We plot the cross-correlation between the first MagLim redshift bin ($0.20 < z < 0.40$) and the red, blue, and total LSBG sample positions in Fig. A1. The measurements are slightly negative at scales of 3-20 arcmin, though this effect is small.

A2 redMaGiC Cross-Correlation

We plot the cross-correlation between the red LSBG sample and the five redMaGiC redshift bins, listed in tab. I of Prat et al. (2022) and spanning from $0.15 < z < 0.90$. The results are shown in Fig. A2

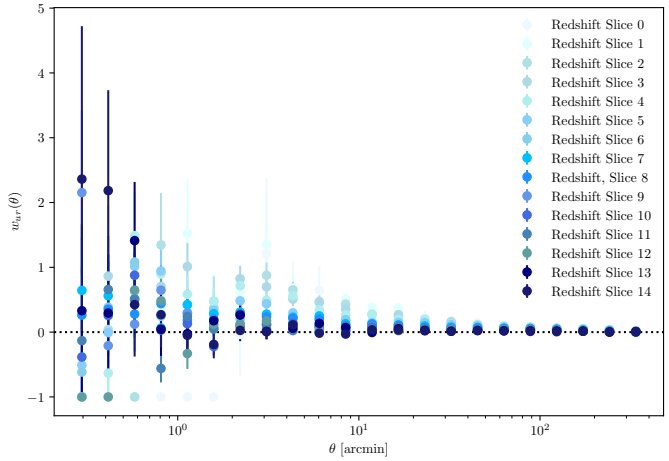

Figure A3. Cross-correlation between the blue LSBG positions and the 2MPZ catalog across angular scales, in 14 redshift slices spanning from 0.0 to 0.14 with a width of 0.01.

A3 Blue LSBG Cross-Correlation

We plot the cross-correlation measurements between the 2MPZ catalog and the blue LSBG sample across angular scales of 0.25-400 arcmin in 14 redshift slices spanning from 0.0 to 0.14 with a width of 0.01. We show the results in Fig. A3.

APPENDIX B: MEASURING GALAXY BIAS

We plot the galaxy bias, measured using the 2MPZ autocorrelation function and the dark-matter two-point correlation function after Eq. 14, as a function of angular scales and redshift. The galaxy bias appears most linear at θ = 16.53 arcmin, θ = 23.13 arcmin, θ = 32.45 arcmin, θ = 45.23 arcmin, and θ = 63.25 arcmin.

APPENDIX C: VALIDATING WIDTH OF THE OFFSET DISTRIBUTION

We include the width of the offset distribution as a parameter and find that this result is consistent with the fiducial model. We list the posteriors in Tab. C1 and display the results in Fig. C2.

Red Galaxies	Priors	Posteriors
Subhalo Mass	U($10^7 M_\odot < M_{\rm sub} < 10^{12} M_\odot$)	$M_{\rm sub} < 2.8 \times 10^{11} M_\odot$
Host Halo Mass	U($10^{10} M_\odot < M_{\rm host} < 10^{15} M_\odot$)	$7.0^{+2.1}_{-1.6} \times 10^{12} M_\odot$
Offset	U(25 arcmin $< \mu <$ 55 arcmin)	$38.9^{+4.5}_{-4.6}$
Offset Distribution Width	U(2 arcmin $< \sigma <$ 25 arcmin)	$11.5^{+4.7}_{-4.7}$ arcmin

Table C1: Priors and mean posteriors for red LSBG tangential shear measurements for the mean radial offset, the width of the offset distribution, and the subhalo mass and host halo mass. These results correspond to Fig. C2.

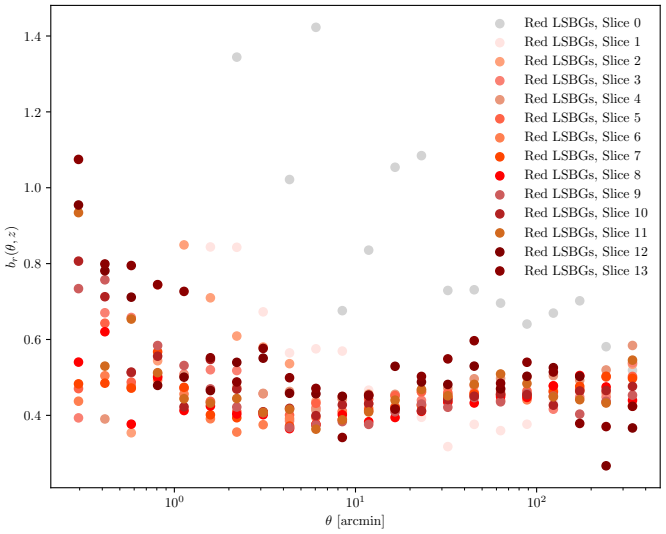

Figure C1.

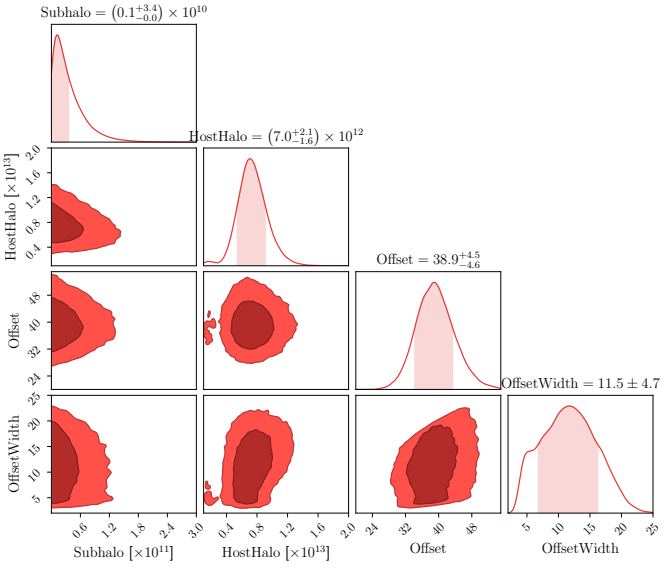

Figure C2. MCMC posterior distribution corresponding to Tab. C1. The width of the offset distribution is included as a parameter.